Diffraction-based Sensitivity Analysis for an External Occulter Laboratory Demonstration

DAN SIRBU[1,2], YUNJONG KIM[1], N. JEREMY KASDIN[1], AND ROBERT J. VANDERBEI[1]

[1] High Contrast Imaging Laboratory, Mechanical & Aerospace Engineering Princeton University, Princeton, NJ, 08544, USA
[2] NASA Ames Research Center, Moffett Field, Mountain View CA, 94035, USA
[*] Corresponding author: *dan.sirbu@nasa.gov

Compiled June 14, 2016

An external flower-shaped occulter flying in formation with a space telescope can theoretically provide sufficient starlight suppression to enable direct imaging of an Earth-like planet. Occulter shapes are scaled to enable experimental validation of their performance at laboratory dimensions. Previous experimental results have shown promising performance but have not realized the full theoretical potential of occulter designs. Here, we develop a two-dimensional diffraction model for optical propagations for occulters incorporating experimental errors. We perform a sensitivity analysis, and comparison with experimental results from a scaled-occulter testbed validates the optical model to the 10^{-10} contrast level. The manufacturing accuracy along the edge of the occulter shape is identified as the limiting factor to achieving the theoretical potential of the occulter design. This hypothesis is experimentally validated using a second occulter mask manufactured with increased edge feature accuracy and resulting in a measured contrast level approaching the 10^{-12} level – a better than one order of magnitude improvement in performance.

OCIS codes: *(050.1380) Binary optics, (220.1230) Apodization (050.1940) Diffraction, (350.6090) Space optics, (120.6085) Space instrumentation, (350.1260) Astronomical optics.*

http://dx.doi.org/10.1364/ao.XX.XXXXXX

1. INTRODUCTION

The direct imaging of an Earth-like planet around a nearby stellar system, or an exo-Earth, is one of the most important scientific goals of astronomy but requires an extraordinary capability for high-contrast imaging. The contrast ratio between the peak of the stellar point spread function (PSF) and that of a modeled exo-Earth in visible and near-IR bands is ten orders of magnitude [1]. Thus, the fainter exo-Earth is located at a small angular separation from its host-star even for the nearest planetary systems to our Sun and would be indistinguishable from the diffraction wings of the stellar PSF.

An exo-Earth high-contrast imaging capability will require use of a starlight suppression system. The external occulter, also referred to as a starshade, was first proposed by Lyman Spitzer in 1962 [2] and is an alternative to an internal coronagraph that does not require an active wavefront control system. An occulter spacecraft is flown in formation with a space-telescope along its line-of-sight to the host star, and prevents most of the starlight from entering the telescope pupil. The residual starlight due to diffraction must be controlled by optimizing the shape of the occulter. Occulter designs proposed for space missions such as EXO-S, THEIA, and NWO [3–5] use binary occulters – fully transmissive or opaque – which approximate a smooth apodization function through N-fold circular symmetry by introducing a set of petals [6]. These designs are typically tens of meters in diameter and operate at tens of thousands of kilometers separation from the space telescope.

A numerical optimization process has been developed for the design of the occulter apodization function [7]. This and other design approaches are based on scalar diffraction theory. Full-scale petals have been built and assembled; their individual edge shape and assembled configuration has been precisely and repeatedly measured to predict their optical performance based on existing manufacturing capabilities [8]. Nonetheless, the performance prediction is also based on scalar diffraction modeling. Because a full-scale occulter cannot be tested on the ground, it is therefore important to experimentally verify the performance of scaled occulters in the laboratory to validate the optical models used for their design and performance prediction at the contrast level required for the space mission.

Previous occulter experiments have demonstrated high-contrast but not to the full potential of the scaled occulter design. Some of these earlier laboratory tests have been limited by phase aberrations due to wavefront errors from collimating optics,

diffraction effects due to the finite extent of the optics and laboratory enclosure or field site, and scattering from the support structure used to suspend the occulter mask [9–11]. At Princeton, we have developed a proof-of-concept testbed (described in detail in Section 2) which seeks to demonstrate the performance of the occulter mask for which the limiting factor is the occulter mask itself rather than such experimental limitations [12, 13].

The principal idea presented in this paper is a two-dimensional scalar diffraction propagation method that allows modeling of many types of experimental errors for external occulters. Simulation results are compared with laboratory results for the validation of the model to a 10^{-10} contrast level. Previous work found the direct two-dimensional evaluation of the Fresnel diffraction integral for occulter optical propagations to be impractically slow [14, 17]. Our approach combines the Matrix Fourier Transform (MFT) propagation method [15] with anti-aliasing of fine structures to make the direct evaluation numerically tractable. Other optical propagation codes [7, 16–19] integrate along the occulter boundary and use analytical estimates of the impact of other types of errors (e.g., phase errors which are not expected to manifest at space-scale but can be a limiting factor for a laboratory experiment). By comparison, our method allows modeling all experimental errors simultaneously and evaluating their combined effect. The main contributions of this paper are:

- introducing a nomenclature in which we distinguish between suppression (at the telescope pupil) and contrast (at the telescope focal plane) and both are measured (Section 2).
- the development of a two-dimensional optical propagation model for external occulters (Section 3). We provide a validation numerical example demonstrating that the model can reproduce results of the commonly-used one-dimensional optical propagation codes (at the 10^{-13} contrast level that the occulter mask is capable of achieving by design).
- the application of this optical propagation model on the Princeton laboratory testbed (Section 4). We perform a sensitivity analysis to identify the effect on contrast performance of individual experimental errors including phase aberrations on the optical surfaces and volumetric scattering, optical axis misalignments, occulter mask tilt, and manufacturing accuracy of the occulter edges. Application of error parameters to levels expected in the laboratory environment results in a good match to experimental results. We demonstrate in simulation that the factor limiting contrast performance (at the 10^{-10} level obtained in the laboratory experiment) is manufacturing accuracy of the occulter mask edges.
- validation of the hypothesis drawn from the sensitivity analysis that performance is limited by edge feature accuracy (Section 5). We perform an experimental demonstration involving an occulter mask manufactured with increased feature accuracy which results in measured suppression and contrast improvements. The measured contrast approaches the 10^{-12} level – better than one order of magnitude improvement in contrast performance.

The paper concludes with a discussion of steps being undertaken for an experimental demonstration operating at conditions better approximating a space-mission (Section 6).

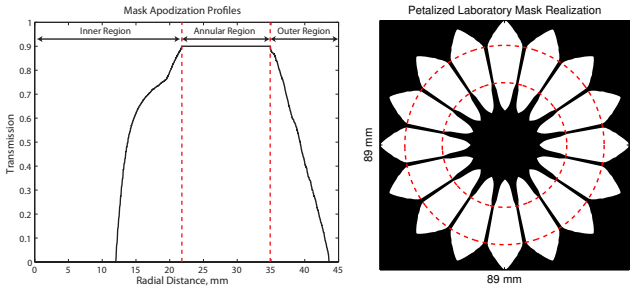

Fig. 1. (a) Optimized occulter apodization profile corresponding to the mask used in the laboratory dimensions. (b) Corresponding binary realization. Inner and outer working angles for the mask are indicated by the dashed lines.

2. EXPERIMENTAL TESTBED AND RESULTS

A. Scaled Occulter Testbed

The apodization profile $A(r)$ used in this experiment is shown in Figure 1a and its petalized realization that comprises the occulter mask is shown in Figure 1b with 0 being fully opaque and 1 fully transmissive. The inner region corresponds to the actual occulter which provides the optimized shadow, whereas the outer region corresponds to an apodized outer ring to mitigate deleterious diffraction effects from mounting the occulter mask and the finite extent of the testbed. The optimized occulter apodization is designed using linear programming methods [7] with the optical propagation applying Babinet's principle [26]. The outer ring apodization is the complement of a similarly-designed oversized occulter. The mask design process and equivalence to the occulter-only design is discussed in more detail in an earlier paper [20].

Because the occulter mask has finite radial extent due to the outer ring the optical propagation does not require use of Babinet's principle. The electric field E_{ap} past an occulter mask with circularly symmetric transmittance profile $A(r)$ at a distance z downstream with wavelength λ, can be written as the Fresnel integral [22]:

$$E_{\text{ap}}(\rho) = \frac{2\pi}{i\lambda z} e^{\frac{\pi i}{\lambda z}\rho^2} \int_0^R e^{\frac{\pi i}{\lambda z}r^2} J_0\left(\frac{2\pi r\rho}{\lambda z}\right) A(r) r dr \qquad (1)$$

where R is the maximal radial extent of the mask, J_0 is the zeroth-order Bessel function of the first kind, ρ is the radial distance across the shadow, and r is the radial distance across the occulter mask. Optimization methods are used to obtain a transmission profile $A(r)$ that produces a shadow with small amplitude magnitude at the pupil plane [7]. Petals (representing N-fold circular symmetry) are a binary approximation of the radial transmission pattern, and their effect is commonly modeled maintaining the one-dimensional integral via a Jacobi-Anger series expansion [7, 17].

Experimental verification of occulters on the ground requires scaling from space dimensions to laboratory dimensions while maintaining a functionally identical optical propagation under relevant conditions. The most common approach for occulter experiments is to introduce a scale factor that keeps the Fresnel numbers ($\frac{r^2}{\lambda z}$ and $\frac{\rho^2}{\lambda z}$) constant, allowing the electric field downstream from the occulter to be re-written identically by making the appropriate substitutions. Additionally, our exper-

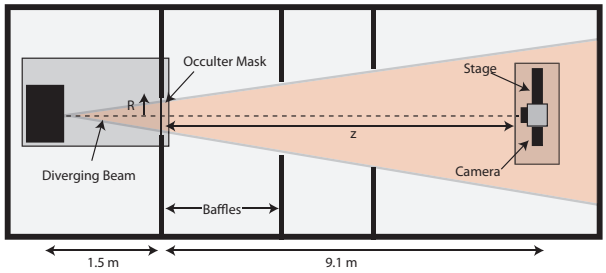

Fig. 2. Schematic of the occulter testbed. The artificial star is incident on an occulter mask with radius R both situated on an optical table on the left-end of the enclosure. The shadow is cast a distance z downstream from the occulter mask on the moveable camera-telescope in the right-end.

iment uses a diverging beam requiring a second scaling step. This two-step scaling process is described mathematically in a previous publication [20] and is shown to result, at laboratory dimensions, in an identical optical propagation equation to the original space dimensions. In this paper we are only concerned with a direct comparison of experimental results to optical model propagations, but make use of this previous scaling derivation to establish equivalence of our results to space scale.

The Fresnel diffraction propagation in Equation 1 is accurate when the following condition is satisfied[22]:

$$z^3 \gg \frac{\pi}{\lambda}(r-\rho)^4_{\max} \tag{2}$$

For space occulters this condition is easily satisfied, as discussed elsewhere in the literature [14]. Under the Fresnel number scaling introduced in the testbed the margin by which the condition is satisfied is reduced. Therefore, an experimental demonstration of a match with a Fresnel-diffraction model in the laboratory regime increases confidence in the validity of modeling space occulters using the Fresnel approximation at the demonstrated suppression levels.

The occulter testbed is shown in Figure 2, and the laboratory parameters are summarized in Table 1. An enclosure measuring 12 m $\times$ 1.2 m $\times$ 2.4 m blocks ambient light. Two passively isolated optical tables are located at each end of the enclosure. The larger optical table contains the optics that create the diverging input beam and the occulter mask. A Deep Reactive Ion Etching (DRIE) process is used to manufacture the mask [21]. The substrate is a 100 mm diameter silicon wafer and the petal openings are etched out. The final sidewall is vertical with a 50 µm thickness. The smaller optical table at the opposite end of the enclosure contains the telescope optics for observations in the occulter mask shadow and consists of a camera mounted on two long-travel stages that provide two degrees of freedom of movement in the plane normal to the optical axis.

The artificial star consists of a single-mode 2 mW HeNe laser operating monochromatically at 632 nm. To create the diverging beam, the beam is passed through two lenses acting as a beam expander, and focused using an off-axis parabolic mirror onto a 15 µm pinhole. The pinhole spatially filters the surface errors on the optics (such aberrations are a limiting factor for collimated occulter experiments; see Section 4 for a simulated demonstration that this is not a factor in our experiment).

We note here this occulter design was generated to fit within the propagation distance available in the testbed. Therefore, compared to a typical occulter design this corresponds to an oversized occulter (i.e., operates at a larger Fresnel number $\approx$ 600, rather than the typical Fresnel number of 10-20). In practice this means that when imaged with the camera-telescope, the occulter appears extremely well resolved compared to what would be expected for a space occulter. This is a beneficial for validating the occulter propagation model as it permits identification of the sources of stray light.

Parameter	Laboratory	Space Equivalent
Pinhole-to-occulter	1.5 m	Infinity
Propagation distance	9.1 m	97,000 km
Radius of dark zone	13 mm	12 m
Occulter diameter	44 mm	380 m
Outer ring diameter	88 mm	N/A
Inner working angle	8.4 arcmin	400 mas
Outer working angle	17 arcmin	800 mas
Telescope diameter	14 mm	17 m
Suppression band	400-1100 nm	400-1100 nm

Table 1. Summary of experimental parameters and their equivalent space scaling.

B. Experimental Results

Following evolving current usage, we propose definitions for two key performance metrics for an occulter-based starlight suppression system. *Suppression* is measured directly at the pupil plane of the telescope. This measurement is taken by first centering the camera in the shadow of the occulter mask without the lens attached and taking long exposures; the mask is then removed and short exposures are taken with suppression obtained as the mean flux ratio between these across the aperture. *Contrast* is measured at the image plane with a camera focused on the artificial star pinhole, and is defined as the ratio between the flux at each pixel in the image formed when the mask is in place and the flux of the peak pixel of the point spread function without a mask. In the occulter literature, these terms are sometimes used interchangeably but it is useful to distinguish between them and measure both.

Figure 3 presents the reduced suppression and contrast experimental data sets obtained from the testbed which will be compared in Section 4 against simulated results from the diffraction model developed in Section 3. In Figure 3a, the contrast-calibrated image plane is shown with the red circles denoting the 400 mas-space equivalent inner and 800 mas-space equivalent outer working angles which define the *annular dark region*. This data-set from [20] is collected to ensure no saturation occurs in individual frames. Calibrated ND filters were used measure the constrast against the bright artificial star. In the annular region, the best azimuthal median contrast recorded was 3.0×10^{-11}, with the worst contrast of 6.3×10^{-9} occuring at the inner 50% throughput angle. We augment the previous contrast data set [20] with the corresponding suppression measurements. Figure 3b, the suppression-calibrated pupil plane mosaic is collected by stitching images collected with the exposed camera CCD at 5 mm intervals. The mean-recorded suppression is 1.4×10^{-5}.

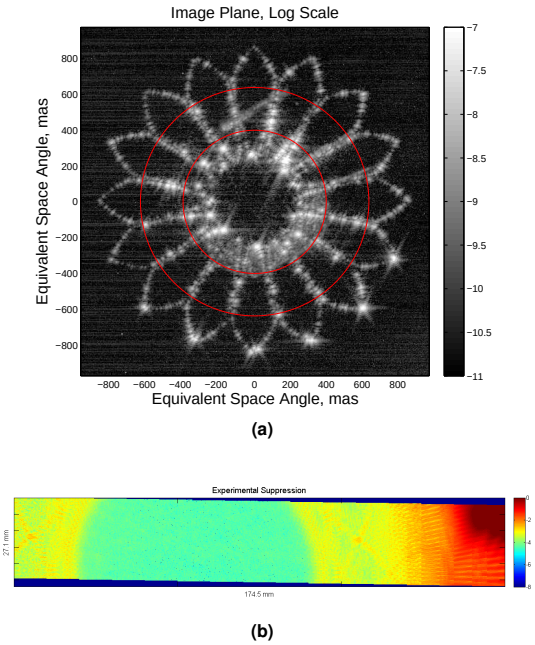

(a)

(b)

Fig. 3. Experimental results obtained from the scaled occulter testbed. (a) Contrast measurements are taken at the image plane. The red lines denote the inner and outer working angles. In the annular dark region, contrast levels are better than 10^{-10}. (b) Suppression measurements are taken at the pupil plane. Here a mosaic is obtained by stitching images at 5mm intervals. Mean suppression across the telescope aperture is 1.5×10^{-5}.

By comparison, the designed (ideal) performance of the occulter mask is better than 10^{-13} contrast in the annular region with the brightest feature at the 50% throughput angle expected to be 1.3×10^{-10}. The corresponding theoretical mean suppression across the aperture is 1.2×10^{-7}.

3. TWO-DIMENSIONAL SCALAR DIFFRACTION MODEL

Here we develop a two-dimensional optical propagation model for obtaining both the suppression at the telescope pupil plane, and the contrast at the telescope focal plane downstream of an occulter mask. This method is direct and intuitive, and by comparison with existing one-dimensional propagation codes allows modeling any type of experimental error directly and assessing combined effects. A numerical example using a high-resolution model that closely approaches the ideal performance of the laboratory occulter mask demonstrating that the model is accurate to very high contrast levels (10^{-13}).

A. Fresnel propagations between optical planes

Figure 4 illustrates propagations between the different planes involved in the occulter testbed. Four optical planes are defined for the occulter testbed: $P0$ is the plane of the pinhole source ($2M \times 2N$ in physical size), $P1$ is the plane of the occulter mask ($2U \times 2V$ in physical size), $P2$ is the pupil plane where the telescope aperture lies and where we measure the suppression of the shadow ($2X \times 2Y$ in physical size), and lastly $P3$ is the focal plane of the telescope and the plane in which we measure the contrast of the point spread function. Thus, to obtain the point spread function of the occulter tesbed three separate Fresnel propagations between these four planes are needed. The numerical method used to perform the Fresnel propagations is MFT-based [15], which reduces the memory requirements compared to a traditional FFT-based propagation.

The first optical propagation occurs between the artificial star source and the occulter mask. The artificial star source has a pinhole with radius r_{pin} across the plane $P0$ spanned by Cartesian coordinates (m, n) and is defined by the following circular function:

$$A_{\text{pin}}(m,n) = \begin{cases} 1, & \sqrt{m^2+n^2} \le r_{\text{pin}} \\ 0, & \text{otherwise.} \end{cases} \tag{3}$$

Then the input electric field at P1 spanned by Cartesian coordinates (u, v) can be computed from a two-dimensional Fresnel integral over the pinhole at P0 as follows:

$$E_{\text{in}}(u,v) = \frac{e^{2\pi i h/\lambda}}{i\lambda h} e^{\frac{\pi i}{\lambda h}(u^2+v^2)} \int_{-N}^{N}\int_{-M}^{M} A_{\text{pin}}(m,n) \, e^{\frac{\pi i}{\lambda h}(m^2+n^2)} e^{-\frac{2\pi i}{\lambda h}(mu+nv)} dmdn \tag{4}$$

where h is the propagation distance between P0 and P1, $-M < m < M$, $-N < n < N$, $-U < u < U$, and $-V < v < V$. This expression for E_{in} assumes a uniform beam across the pinhole, but other profiles such as Gaussian can be chosen.

Next, the Fresnel propagation past the occulter mask represents the main diffractive propagation computing the shadow at $P2$ spanned by Cartesian coordinates (x, y). We use a 2D mask with transmission profile $A(u, v)$ that represents the diffractive effect of the occulter mask. The resulting 2D Fresnel propagation integral between the occulter plane at $P1$ and the telescope's pupil at $P2$ is as follows:

$$E_{\text{pup}}(x,y) = \frac{e^{2\pi i z/\lambda}}{i\lambda z} e^{\frac{\pi i}{\lambda z}(x^2+y^2)} \int_{-V}^{V}\int_{-U}^{U} E_{\text{in}}(u,v) \, A(u,v) e^{\frac{\pi i}{\lambda z}(u^2+v^2)} e^{-\frac{2\pi i}{\lambda z}(ux+vy)} dudv \tag{5}$$

where z is the propagation distance between $P1$ and $P2$, E_{in} is the output of the propagation in Equation 4, $-X < x < X$, and $-Y < y < Y$.

Finally, to propagate from the pupil plane at $P2$ to the image plane at $P3$ a quadratic phase function corresponding to a lens is introduced. Then, a Fresnel propagation is necessary that corresponds to a distance s derived from the thin lens equation taking into account the focal length f of the lens and the distance d to the pinhole that the focus of the lens is set to:

$$E_{\text{im}}(\xi,\eta) = \frac{1}{i\lambda s} \int_{-Y}^{Y}\int_{-X}^{X} E_{\text{pup}}(x,y) A_{\text{pup}}(x,y) \, e^{\frac{-\pi i}{\lambda d}(x^2+y^2)} e^{\frac{-2\pi i}{\lambda s}(x\xi+y\eta)} dxdy \tag{6}$$

where A_{pup} is a circular function (similar to Equation 3) of radius matching the telescope's aperture, E_{pup} is the output of the propagation in Equation 5, and (ξ, η) are Cartesian coordinates spanning the image plane $P3$.

To normalize the intensity at the pupil plane in terms of suppression or the intensity at the image plane in terms of contrast, we set $A(u, v) = 1$ and obtain $\hat{E}_{\text{pup}}(x, y)$ as the electric field output of Equation 5 with no occulter mask in place and $\hat{E}_{\text{im}}(\xi, \eta)$ as the corresponding electric field at the image plane from Equation 6. Then the suppression and contrast metrics are defined as

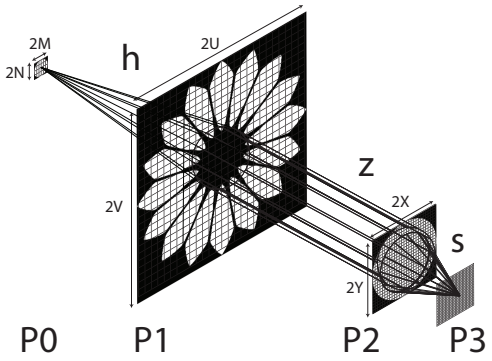

Fig. 4. Optical planes for the occulter testbed. The diverging beam originates from the pinhole at plane P0 and is incident on the occulter mask at plane $P1$. The shadow is directly measured at plane $P2$ in terms of *suppression*, and the point-spread function of the system is measured at $P3$ in terms of *contrast*. Plane physical sizes are indicated, for example 2M x 2N is the size of plane P0.

follows:

$$\text{Supp.}(x,y) = \frac{\left|E_{\text{pup}}(x,y)\right|^2}{\max\left|\hat{E}_{\text{pup}}(x,y)\right|^2} \tag{7}$$

$$\text{Cont.}(\xi,\eta) = \frac{\left|E_{\text{im}}(\xi,\eta)\right|^2}{\max\left|\hat{E}_{\text{im}}(\xi,\eta)\right|^2} \tag{8}$$

Note that throughout the paper, a single suppression value is quoted which is the averaged suppression across the telescope-camera aperture. This is because across the aperture in the dark hole, the shadow has a relatively constant profile. On the other hand, contrast can vary greatly between the occulter edges and the annular dark region.

B. Occulter mask model generation

The mask manufacturing accuracy is modeled by a rectangular grid discretization across the occulter at plane P1. Figure 5 illustrates the process of generating a two-dimensional occulter mask from the one-dimensional apodization profile.

The mask model is incorporated via the term $A(u,v)$ in Equation 5. $A(u,v)$ is set to *white*, or 1, in open areas in which light is allowed to pass and to *black*, or 0, in areas where the binary mask completely blocks light. To generate a binary mask we follow the procedure: 1) generate an $n \times n$ grid; 2) determine polar coordinates of the midpoint of each grid point; 3) compute the radial and angular coordinates of a petal edge; 4) for each midpoint, compute the angular coordinate in relation to the nearest petal center; 5) determine whether each midpoint is a point on the mask (black) or an opening (white) by comparison to the nearest petal edge angular coordinate.

In Figure 5a, this process is shown graphically. A number of test points $p1 - p7$ are chosen that lie on the mask. These test points all have angular coordinates with respect to the petal center that are above the petal edge and are therefore set to black; the shaded area is above the petal edge and represents points on the mask that are fully opaque. Test points $p8 - p12$ have angular coordinates smaller than the petal edge and are therefore set to white and represent the petal openings; the entire white area is below the petal edge and represents points not on the mask that are fully transparent.

We borrow a common spatial anti-aliasing technique to reduce the number of grid points necessary to represent the occulter mask. $A(u,v)$ is allowed to take on gray values over the range $[0,1]$ along the edges of the occulter mask to approximate a higher-resolution grid than can be numerically tractable to fully simulate as a binary mask. This is achieved by computing a pattern of white and black squares over an area and determining the black fraction of the total area to obtain a gray approximation. An example of this spatial anti-aliasing technique applied to the treatment of the occulter edges is shown in Figure 5b.

Thus, a mask of radius R with $n \times n$ samples which uses a $g \times g$ anti-aliasing approximates a mask with feature size of $\delta R = 2R/n/g$, where R is the radius of the mask to the outer edge. Such a mask with feature size $\delta R = 0.55$ µm is shown in Figure 5c.

Note that the discretization parameter δR is only a proxy, or an approximation, of the true feature size of the occulter mask manufacturing process. The occulter mask design is manufactured by specifying a set of points along the occulter edge. The spacing between these points is what we call the manufacturing process *feature size*. A petal tip detail realization for two different feature sizes is shown in Figure 6 and illustrates the effect of a ten-fold improvement in manufacturing feature size.

C. Numerical example

To demonstrate the accuracy of this diffraction model, a detailed mask model is generated as shown in Figure 5c with $n = 16{,}000$, $g = 10$. At laboratory dimensions, this discretization approximates a feature size of $\delta R = 0.55$ µm. The two-dimensional propagation to the image plane for this high-resolution mask is compared against the one-dimensional propagation of the designed apodization profile representing the case of perfect feature accuracy.

To compute the theoretical performance of a petalized occulter mask, a 1D propagation Fresnel diffraction integral has typically been used with a Jacobi-Anger expansion resulting in a series summation providing the ideal contribution from the petals as introduced in [7]. This represents the ideal performance of this testbed as designed. The computed contrast in the image plane is shown in Figure 7a, and the corresponding computed mean suppression across the telescope pupil is $10^{-6.91}$. The contrast in the annular working region reaches the 10^{-13} level.

Using the high-resolution 2D mask model from Figure 5c, the computed contrast result is shown in Figure 7b and attains a corresponding $10^{-6.60}$ mean suppression measurement, and the contrast in the annular working zone also reaches the 10^{-13} level. This comparison demonstrates that a mask with sufficiently high resolution can approach the ideal performance of the occulter mask as realized with 16-petals and validates the accuracy of the 2D propagation model to a deep contrast level.

4. SENSITIVITY ANALYSIS

The propagation model presented in the previous section does not contain any errors except for discretization from the occulter mask grid. We can use this model to introduce many types of experimental errors individually, and combine these at expected laboratory levels.

In the pupil plane, the suppression of the experimental mask levels off across the dark hole (see in Figure 3b). The image plane results shown in Figure 3a identify the provenance of the additional light leakage. The bright edges are most likely caused by diffraction from departures from the ideal occulter

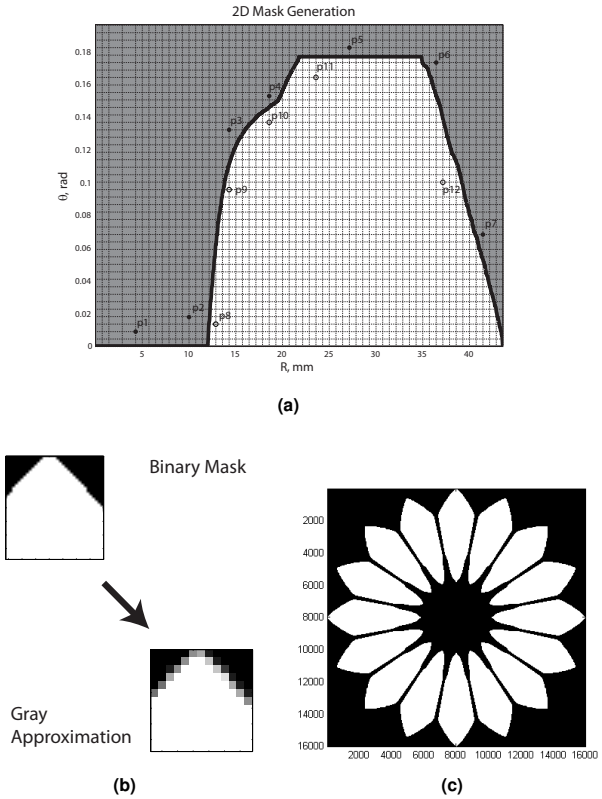

Fig. 5. Generation of the two–dimensional apodization profile $A(u, v)$. (a) the one dimensional radial apodization profile is converted to a half-petal edge. Filled test points p1-p7 have angular coordinate θ greater than the nearest edge point and therefore lie on the mask. The entire shaded area lies on the mask. Empty test points p8-p12 have θ smaller than edge are therefore part of the petal openings. The entire white area consists of mask openings. (b) tip section demonstrating anti-aliasing procedure to obtain a gray approximation at the edges of the mask; (c) resulting 2D mask model using 16,000 $\times$ 16,000 points, and a 10 $\times$ 10 anti-aliasing, representing feature size of $\delta R = 0.55$ µm.

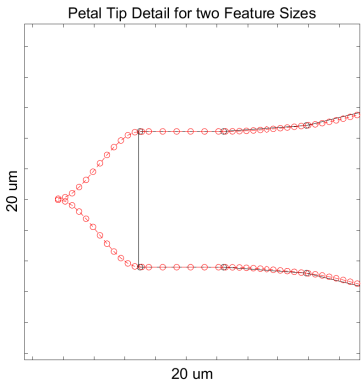

Fig. 6. Comparison of inner petal tip detail realization for a mask with two average feature sizes: 0.5 µm is shown in red and 5 µm is shown in black.

shape (for example localized manufacturing defects in the form

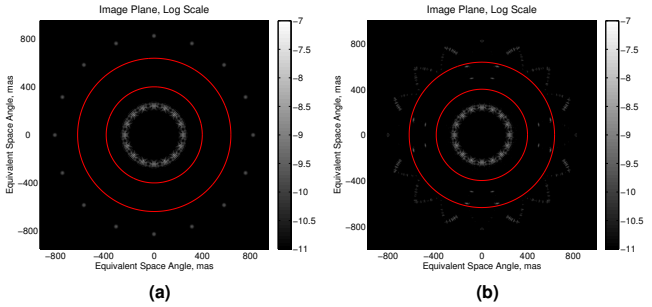

Fig. 7. Comparison of ideal model with finite feature-size limited model (a) Theoretical contrast at the image plane using the 1D binary propagation. Corresponding suppression is 2.0×10^{-7}. The inner and outer red circles denote the annular dark region. (b) Theoretical contrast at the image plane using a 2D propagation with a high-resolution mask featuring 0.55 µm feature size. Corresponding suppression is 2.5×10^{-7}.

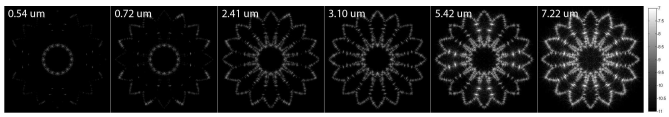

Fig. 8. Contrast as a function of grid discretization (an approximation for manufacturing feature size).

of over or under-etching). Misalignment of the input beam manifests as a bright ring around the inner occulter mask. Air currents can produce phase shifts across the aperture while surface aberrations from the artificial star optics are expected to be filtered by the pinhole (a limiting effect for collimated experiments).

A. Manufacturing process feature size

When converting the mask's apodization profile for CAD specifications for etching of the silicon wafer, the output consists of 16 different sets of points with each defining a polygon petal opening of the occulter mask. The spacing of points along the petal edges represents the accuracy with which the polygon is defined – a small number of points results in longer straight edges which can introduce additional diffraction leakage along the occulter edges.

For the 2D diffraction model previously described in Section 3, the manufacturing process δR feature size can be approximated by choice of the discretization grid of the occulter mask via the number of sampling points n and the number of anti-aliasing points g. A number of different occulter mask models are generated to represent masks with different uniform feature sizes.

Using these mask models across the occulter plane $P1$, we perform optical propagations and compare these to the high-resolution mask performance. Figure 8 shows the contrast-calibrated image plane results as the manufacturing feature size is worsened. Suppression performance across the dark hole is reduced from 2.5×10^{-7} for the high-resolution mask to 4.1×10^{-5} in the worst case shown. The corresponding contrast across the dark annular regions in the image plane is decreased from 7.8×10^{-13} to 3.9×10^{-11}.

Qualitatively we can see in the image plane that the edge

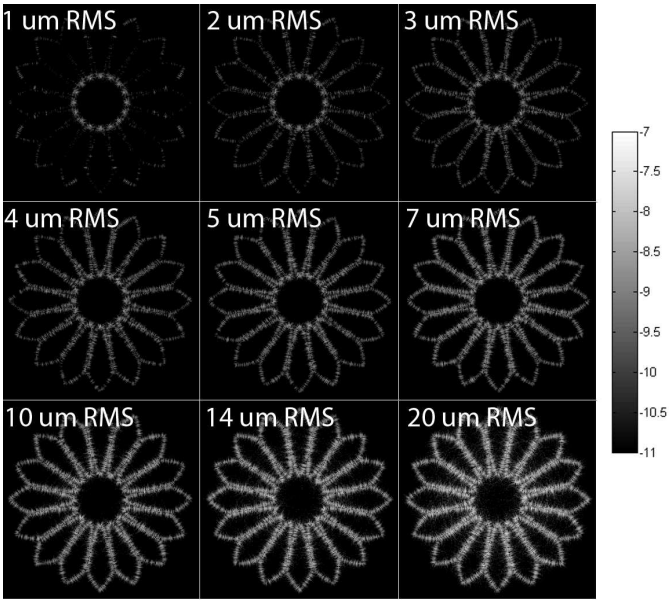

Fig. 9. Contrast as a function of statistical edge deviation from theoretical.

diffraction is significantly increased resulting in bright edges across the occulter mask similar to those seen experimentally in Figure 3a. A clear trend in Figure 8 is that larger feature size results in significantly more diffraction across the mask edges than predicted from the perfect petal realization expected from the ideal theoretical performance.

B. Edge perturbations

The resulting two-dimensional mask $A(u,v)$ after choice of discretization parameter is symmetrical (except for discretization errors arising from representation of a 16-fold circularly symmetric pattern onto a two-dimensional grid). To remove symmetry and simulate manufacturing variations between different petals of the occulter mask, a set of circular defects are added along the petal edge. These defects can either be under-etching (reduction in transmission) or over-etching (increase in transmission).

To obtain an estimate of the amount of perturbation to realistically introduce in the model, we performed spot miscroscope imaging of the occulter mask. The procedure to obtain the microscope images and fit them to the designed occulter edges are described in more detail in [13, 24]. The deviation between the measured edge and the theoretical contour is obtained for each measured point along the extracted edge and we obtained an estimated root-mean-square (RMS) value of 3.1 µm.

The edge perturbation model consists of a set of circular defects that are added (for under-etching) or subtracted (for over-etching) from the occulter mask's edge. We first identify 16 different sets of continuous gray contour grid points indexed by k corresponding to individual petals $C^k = \left\{ c^k \,\middle|\, 0 < c^k < 1, c \in \mathbb{R} \right\}$ with each set containing N_k elements representing the total number of grid points along the petal contour.

Reference [25] describes a procedure to generate a stochastic sequence with a specified variance and frequency envelope. Following this procedure, 16 separate stochastic sequences are generated with a flat frequency envelope (white noise) and a 3.1 µm root-mean square, with each edge perturbation set denoted as $E^k = \left\{ e^k \,\middle|\, e^k \in \mathbb{R} \right\}$. As with the contour set C^k, each edge perturbation set E^k contains N_k elements. Each individual entry e_i^k (with i the indexing variable across the set E^k) represents the radius of one circular defect.

Next, the set of circular defects is injected onto the original petal contour. The set of pixels along the petal representing the occulter edge is $\bar{C}^k = \left\{ \bar{c}^k \,\middle|\, 0 \le \bar{c}^k \le 1, \bar{c}^k \in \mathbb{R} \right\}$ for each petal k. The contribution from the sequence of circular defects is added to the original petal contours:

$$\bar{c}_i^k = c_i^k + \frac{\pi (e_i^k)^2}{(n\delta R)^2}, \qquad \forall i \in \{1 \dots N_k\} \tag{9}$$

For large circular defects, the condition $0 \le \bar{c}_i^k \le 1$ avoids unphysical effects. The large defect is instead bled into neighboring pixels by estimating the fractional area that the defect spans across these pixels.

Figure 9 shows the contrast-calibrated image plane results for the high-resolution occulter mask with increasing amounts of root-mean-square edge perturbations injected as described. Qualitatively, with increasing edge perturbations there is increased diffraction leakage along the occulter edges. Diffraction from the edges is also very uniform, a consequence of the white-noise structure of the injected perturbations.

C. Input beam modeling

The non-uniform amplitude profile of a Gaussian beam across the pinhole coupled with displacement of the optical axis of the pinhole from the occulter plane to simulate optical misalignment is a departure from the uniform amplitude profile assumed as illuminating the occulter for the original space design. Additionally, we adopted a diverging beam to eliminate optical aberations from optical surfaces. Therefore, it is important to investigate the sensitivity at laboratory conditions for all such input beam errors.

To account for the Gaussian beam and optical aberrations across the pinhole, a modification of Equation 4, which was written for a uniform beam across the pinhole, introduces two additional multiplicative terms inside the integral

$$E_{\text{in}}(u,v) = \frac{e^{2\pi i h/\lambda}}{i\lambda h} e^{\frac{\pi i}{\lambda h}(u^2+v^2)} \int_{-N}^{N}\int_{-M}^{M} E_{\text{beam}}(m,n) e^{i\phi_{\text{pin}}(m,n)} A_{\text{pin}}(m,n) e^{\frac{\pi i}{\lambda h}(m^2+n^2)} e^{-\frac{2\pi i}{\lambda h}(mu+nv)} dm dn \tag{10}$$

where $\phi_{\text{pin}}(m,n)$ are the phase aberrations introduced by the folding mirror and focusing optics, simulated as pure phase aberrations collocated at the pinhole plane. A circularly symmetric Gaussian beam can be written at the pinhole plane as:

$$E_{\text{beam}}(m,n) = e^{-\frac{\pi i}{\lambda}\frac{\sqrt{m^2+n^2}}{q}} \tag{11}$$

The complex beam parameter q and ABCD ray transfer matrices relate q at the laser focus with propagation through free-space and subsequent focusing. The resulting Gaussian beam profile across the 15 µm diameter pinhole features added phase aberrations from the upstream optics (which have surface quality of root-mean-square $\lambda/4$). Lastly, displacement of the input pinhole center with respect to the occulter mask simulates misalignment of directions transverse to the optical axis (note that occulters are very robust to misalignments along the optical axis).

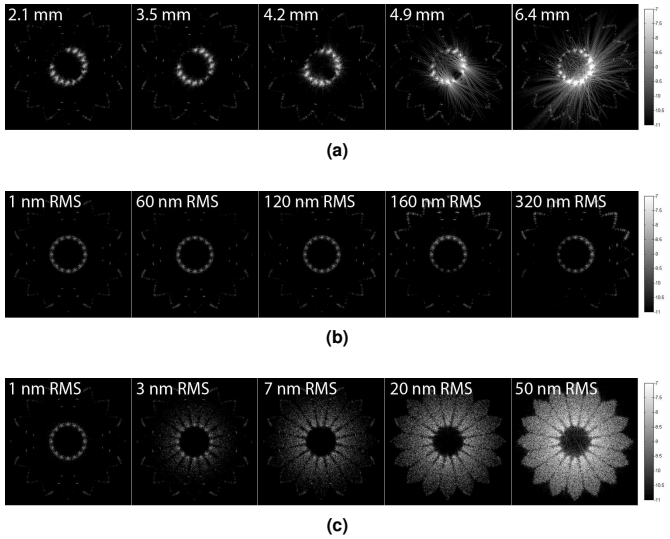

Fig. 10. Contrast sensitivity to (a) diagonal input beam displacement, (b) aberrations from the upstream optics, and (c) wavefront errors applied directly at the occulter plane.

In Figure 10, contrast-calibrated image plane sensitivity analysis results are shown. First, an increasing beam misalignment in the diagonal direction is shown in Figure 10a. This results in light leakage around the central portion of the mask as seen experimentally, with performance relatively robust until there is a clear misalignment and a large amount of light leaks around the central occulter mask.

Next, pure phase aberrations are added across the pinhole plane P0. The results shown in Figure 10b correspond to increasing phase aberrations. These aberrations are produced following the procedure described for generating the one-dimensional random edge perturbations with two main differences: a two-dimensional aberrated matrix is output instead of a one-dimensional sequence, and instead of a flat frequency envelope used for white noise we colored noise with a frequency envelope of $1/f^{\alpha}$ where $\alpha = 3/2$ typical of optical surface errors. Because of the spatial filtering effect of the pinhole, high-frequency phase aberrations from the optics are filtered and only low-order aberrations such as tip-tilt remain. These can be clearly seen in the image plane results for large aberrations on the order of $\lambda/4$ or greater, but these have a small effect on the performance. For example, the worst suppression is only 3.0×10^{-7} compared to an unaberrated suppression of 2.5×10^{-7}.

This model can demonstrate the deleterious effect of phase errors on the occulter mask, thus validating the choice of a diverging beam in this experiment. We introduce stochastic phase errors collocated at the occulter plane P1 with a frequency envelope of $f^{-3/2}$ describing optical surface errors. The sensitivity to stochastic phase errors at the occulter mask plane with increasing root-mean-square is shown in Figure 10c. In this experiment, volumetric scattering from propagation through air (rather than vacuum) can introduce aberrations between the pinhole and the occulter plane. These were expected to be insignificant because of the short distance between the pinhole and the occulter mask. Comparison of the experimental contrast figure in Figure 3a confirms that the provenance of the light leakage is from the occulter edges and not from the openings (as seen in the sensitivity simulations here).

Table 2. Summary of realistic error parameters for diffractive simulation of laboratory environment.

Error Parameter	Estimated Value
Feature size, δR	2.4 µm
Edge perturbations	3.1 µm RMS
Optics aberrations, $\sigma_{\text{pin,RMS}}$	$\lambda/4 \approx 160$ nm RMS
Wavefront aberrations, $\sigma_{\text{occ,RMS}}$	3 nm RMS
Camera aberrations, $\sigma_{\text{cam,RMS}}$	30 nm RMS
Diagonal beam misalignment	4.1 mm
Mask tilt	5°

D. Mask tilt

The occulter mask is tilted at a 5° angle to ensure a ghost reflection does not back-propagate into the occulter plane. Previous tolerancing studies have shown that occulters are tolerant of out-of-plane tilts [19, 23]. These studies have applied a tilt on the shadow which is a good first-order approximation, but using the two-dimensional mask model we can model the loss of symmetry directly due to the mask tilt (and combine this with other errors) by rotation and in-plane projection of the occulter mask.

Figure 11 shows contrast-calibrated image plane results for increasing mask tilts. Performance of the mask is very robust to the loss of amplitude symmetry due to the mask tilt. Suppression performance only decreases to 3.3×10^{-7} for a 20° tilt (compared to an unaberrated 2.5×10^{-7} suppression). There is more variation for contrast levels across the dark annular regions than is directly apparent from the suppression measure, primarily arising due to the elliptical change of the image shape.

E. Camera model

We have developed a camera model to apply realistic measurement errors in simulations. The camera model consists of inclusion of: (1) optical aberrations on the imaging lens and (2) shot noise injected into the simulated image.

We have added optical aberrations on the simulated camera lens. These aberrations are generated similarly to the phase aberrations described previously in Section C with a given standard deviation σ_{cam} and a decreasing $f^{-3/2}$ frequency ramp representative of optical aberrations. These are added as an additional phase term across the camera pupil at plane P2 in Equation 6. In Figure 12, we show the effect on the image plane as the standard deviation of the phase aberrations added across the lens is increased. The aberrations must be very large to be domi-

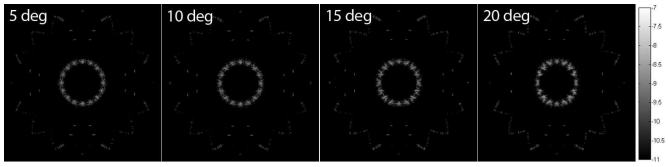

Fig. 11. Contrast as a function of mask tilt

nating. For expected aberrations of $\lambda/4$ or smaller the effect of introducing phase aberrations on the camera telescope is not significant; this demonstates what has been widely considered to be a strength of external occulters, that is insensitivity to the optical quality on the telescope [4].

Inclusion of camera noise is particularly relevant to the contrast-calibrated image-plane simulations which feature high-dynamic range between the glowing occulter edges and the dark regions between the petals. The effect of dark current and read noise is estimated from the variance of contrast-calibrated reduced camera dark frames. Gaussian noise is then injected into the simulated image with the corresponding measured variance.

F. Comparison to experimental results

All the different modeled errors can be combined in one optical propagation to assess the diffractive model performance of the occulter mask in the laboratory environment. Realistic parameters for the laboratory environment are listed in Table 2. The feature and edge accuracy match spot microscope images. Additionally, it is known that the mask does not have fully uniform feature sizes – these increase at the inner and outer tips where the apodization changes most rapidly. We introduce radially-dependent perturbation of the edges (using Equation 9) to match these larger feature changes. The mask tilt is a measured laboratory parameter. The phase aberrations across the pinhole are due to the vendor-quoted surface quality of the upstream optics. The beam displacement is measured from the experimental image plane results. Wavefront aberrations across the occulter plane are unknown, however, a small value is applied as it can be inferred from a qualitative comparison of the experimental results to the sensitivity analysis that the wavefront aberrations are not limiting suppression. Finally, camera aberrations under $\lambda/4$ are negligible.

Figure 13 compares a contrast-calibrated image plane derived from the simulated optical propagation including all the modeled errors in Figure 13a with the experimental results (previously shown in Figure 3a) side-by-side for ease of comparison.

For a more quantitative comparison, the azimuthal cross-sections of contrast-calibrated image plane results are shown in Figure 14 and we also include the theoretical curve for the ideal, unaberrated 16-fold circular realization corresponding to Figure 7a. As can be seen from the figure, the introduction of error parameters corresponding to the expected values in the testbed demonstrates good agreement to the measured contrast curve. The dominating factor in terms of performance is the combination of finite feature sizes in the manufacturing of the mask and deviations from the prescribed ideal shape.

Some of the errors introduced, including the edge perturbations, the optical train aberrations prior to the pinhole, and phase aberrations collocated at the occulter plane are stochastic errors. The occulter performance can vary between simulations. We therefore perform a Monte Carlo assessment using a larger number of simulations with stochastic errors generated randomly for each of the aberrations described above. Such an ensemble of simulations gives a better assessment of the variation of the performance of the occulter than a single simulation. In Figure 15 we show the suppression results from a set of 100 simulations at 633 nm that provides an estimate of the expected suppression distribution. The suppression results are placed into ten equally sized bins, with the simulation frequency indicated. The probability density function (PDF) of the expected suppression performance is reconstructed from the simulated suppression results through normal kernel density estimates [27, 28] (using the `ksdensity` function in MATLAB's Statistics toolbox). We can obtain quantitative estimates of the simulated suppression performance by computing the cumulative distribution function (CDF). From the CDF, we find the expected model suppression to be 1.0×10^{-5} with a confidence interval given by 7.8×10^{-6} at the 5th percentile and 1.7×10^{-5} at the 95th percentiles.

Thus, for expected laboratory parameters, the measured suppression performance falls within the simulated distribution. The contrast curves are well matched at the peaks which dominate the measured suppression. The limiting factor is primarily

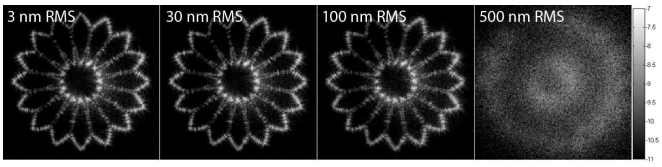

Fig. 12. Contrast as a function of camera lens aberrations.

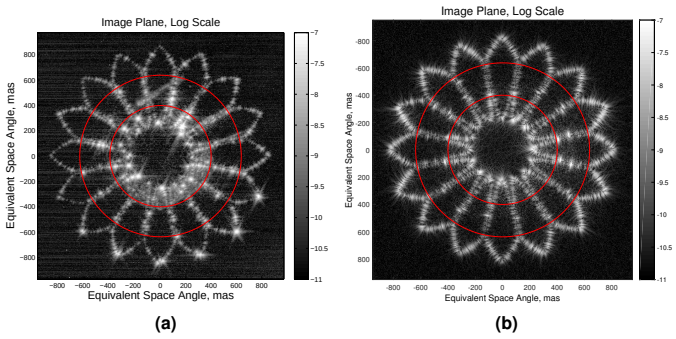

Fig. 13. (a) Experimental contrast at image plane. Corresponding measured suppression 1.5×10^{-5}. (b) Diffractive analysis with experimental errors. Corresponding modeled suppression 1.7×10^{-5}.

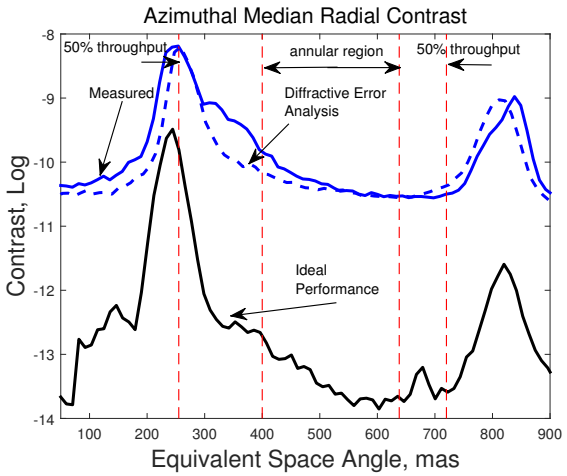

Fig. 14. Azimuthal median cross-section comparison between the experimental results, the theoretical performance of the idealized occulter mask, and the performance with the diffractive modeled error sources included.

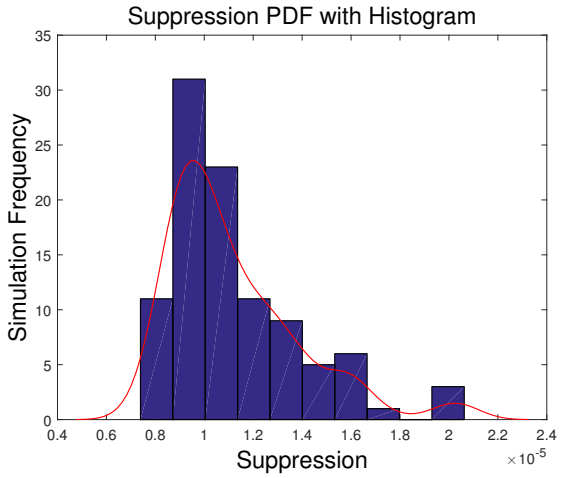

Fig. 15. Suppression performance for a Monte Carlo analysis using 100 simulations at 633 nm and the corresponding probability density function. Expected suppression performance is 1.0×10^{-5}. The 5th percentile suppression is 7.8×10^{-6} and the 95th percentile suppression is 1.7×10^{-5}. The measured suppression of 1.5×10^{-5} falls within the 95% confidence interval.

diffraction from the mask edges due to manufacturing errors.

5. EXPERIMENTAL VALIDATION

To validate the hypothesis of the sensitivity analysis in the previous section, we have manufactured an improved occulter mask using better edge feature accuracy and smaller deviations from the prescribed shape and tested this new mask in the testbed. This required changing the original DRIE process with electron beam lithography and further thinning of the sidewalls, necessary to better control the edge feature accuracy. This improved manufacturing process has been developed primarily for coronagraph masks for the WFIRST mission and is described in more detail elsewhere [29].

The improved occulter mask corresponds to the same occulter design; however, additional points are prescribed along the edges of the occulter mask in order to increase the feature accuracy. When necessary, additional points are added to create a more uniform distribution of straight edges. This occulter mask features an average 0.5 µm feature accuracy with an estimated 0.2 µm RMS edge pertubation. The experimental measurement procedure is identical to that described in Section 2 with the only difference being a substitution of the original occulter mask.

The reduced contrast results corresponding to the increased feature accuracy mask are compared in Figure 16. Figure 16a shows the experimental results and Figure 16b shows the corresponding simulation results. We compare the azimuthal cross-sections in Figure 17, indicating the experimental measurements for the original occulter mask and the occulter mask with improved feature accuracy. The diffractive error analysis is well-matched especially at the inner-working angle peak and the trough; at the outer edges we see some qualitative differences in the morphology of the edge scatter. The experimental contrast performance approaches the 10^{-12} contrast level and is better than an order of magnitude improvement compared to the original mask. The measured suppression improves from 1.5×10^{-5} to 6.0×10^{-6}. This experimental demonstration shows that the limiting factor is the edge feature accuracy of the occulter mask

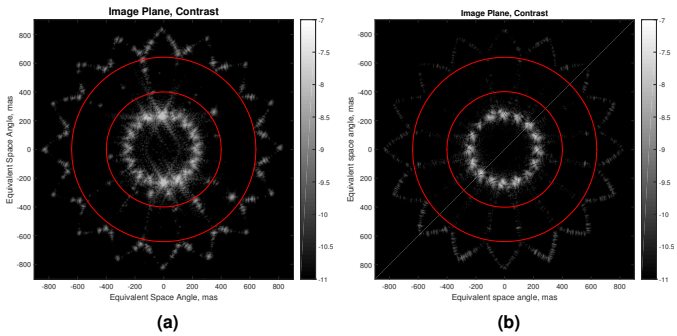

Fig. 16. (a) Experimental contrast at image plane for the occulter mask with improved feature accuracy. Corresponding measured suppression is 6.0×10^{-6} (b) Simulated contrast at the image plane.

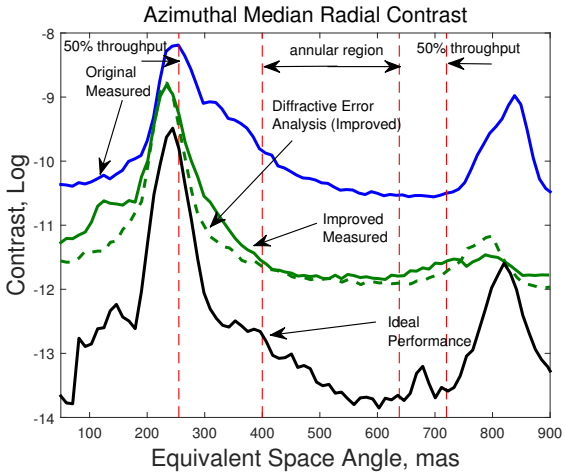

Fig. 17. Azimuthal median cross-section comparison between the experimental results corresponding to the original mask (solid blue) with the experimental results corresponding to the mask featuring improved feature accuracy (solid green). These are compared with the theoretical performance of the idealized occulter mask (black) and the performance with the diffractive modeled error sources for the improved feature accuracy mask (dashed green).

as predicted from the earlier sensitivity analysis.

6. CONCLUSIONS

In this paper, we have proposed a direct two-dimensional Fresnel diffraction model to evaluate occulter performance. We have shown that this model is able to replicate the ideal, unaberrated performance predicted by existing one-dimensional propagation codes at the 10^{-13} contrast level and the 10^{-7} suppression level. Additionally, we have compared the model against experimental data and were able to replicate measured contrast to a level better than 10^{-10} and suppression to a level approaching 10^{-5} using a combination of errors with parameters matching expected laboratory levels.

This analysis has also shown that the dominating error terms for the testbed are occulter edge effects. An experimental validation of the hypothesis drawn from the sensitivity analysis demonstrated that manufacturing improvements in the edge

feature accuracy of the occulter mask improve both measured contrast and suppression performance. The measured contrast level is approaching the 10^{-12} level and represents a better than one order of magnitude improvement compared to the original occulter mask, while the suppression level improved by a factor of 2.5.

For an experimental demonstration of occulter performance at a space geometry, we will need to operate at much smaller Fresnel numbers (in the range of 10-20). The current testbed is limited in terms of the propagation distance, but we have used our experimentally-verified diffraction model to design and predict the performance of a more realistic testbed operating at typical flight Fresnel numbers by expanding the testbed propagation distance [13, 30]. In the existing testbed the enclosure was oversized guaranteeing no deleterious diffraction effects. For an extended testbed this will not be possible due to the larger propagation distances involved. We have found the diffraction model presented here useful for estimating the effect of a type of experimental error previously unmodelled – diffraction effects due to the finite tunnel size which will be the subject of a future communication. This extended testbed is currently under construction at Princeton [31], and when operational it will enable experimental measurements of suppression approaching 10^{-9} while maintaining contrast better than 10^{-10} as required for exo-Earth imaging.

FUNDING INFORMATION

This work was partially performed under NASA contract NNX09AB97G and grant 1430187 from the California Institute of Technology's Jet Propulsion Laboratory. DS acknowledges financial support from the NASA Earth & Space Science Fellowship and the Natural Sciences and Engineering Research Council of Canada postgraduate scholarship.

ACKNOWLEDGMENTS

We thank Bala Balasubramanian, Eric Cady, Pierre Echternach, Tyler Groff, AJ Riggs, Stuart Shaklan, and Victor White for many helpful discussions. We also thank the two reviewers for comments that helped simplify the exposition of the results in this paper.

REFERENCES

1. D. Des Marais, M. Harwit, K. Jucks, J. Kasting, D. Lin, J. Kunine, J. Schneider, S. Seager, W. Traub, and N. Woolf, "Remote sensing of planetary properties and biosignatures on extrasolar terrestrial planets," Astrobiology **2**, 153-181 (2002).
2. L. Spitzer, "The beginnings and future of space astronomy," Am. Sci. **50**, 473-484 (1962).
3. S. Seager, M. Turnbull, D. Lisman, W. Sparks, D. Webb, S. Shaklan, M. Thomson, R. Trabert, and N. J. Kasdin, "EXO-S: starshade probe-class exoplanet direct imaging mission concept," White Paper (2015).
4. N. J. Kasdin, E. Cady, P. Dumont, P. Lisman, S. Shaklan, R. Soummer, D. Spergel, and R. Vanderbei, "Occulter design for THEIA," Proc. SPIE **7440**, 744005 (2009).
5. W. Cash, "Detection of earth-like planets around nearby stars using a petal-shaped occulter," Nature **442**, 51-53 (2006).
6. R. Vanderbei, D. Spergel, and N. J. Kasdin, "Circularly symmetric apodization via star-shaped masks," Astrophys. J. **599**, 686-694 (2003).
7. R. Vanderbei, E. Cady, and N. J. Kasdin, "Optimal occulter design for finding extrasolar planets," Astrophys. J. **665**, 794-798 (2007).
8. N. J. Kasdin, R. Vanderbei, D. Sirbu, J. Samuels, S. Shaklan, D. Lisman, M. Thomson, E. Cady, S. Martin, "Recent progress on external occulter technology for imaging exosolar planets," in *Proceedings of IEEE Aerospace Conference* (IEEE, 2013).
9. E. Schindhelm, A. Shipley, P. Oakley, D. Leviton, W. Cash, and G. Card, "Laboratory studies of petal-shaped occulters, " Proc. SPIE **6693**, 669305 (2007).
10. R. Samuele, R. Varshneya, T. Johnson, A. Johnson, and T. Glassman, "Progress at the starshade testbed at Northrop Grumman Aerospace Systems – comparisons with computer simulations, " Proc. SPIE **7731**, 773151 (2010).
11. T. Glassman, S. Casement, S. Warwick, and M. Novicki, "Measurements of high-contrast starshade performance ", Proc. SPIE **9143**, 91432O (2014).
12. E. Cady, K. Balasubramanian, M. Carr, M. Dickie, P. Echternach, N.J. Kasdin, S. Shaklan, D. Sirbu and V. White, "Broadband suppression and occulter position sensing at the Princeton occulter testbed," Proc. SPIE **7731**, 77312F (2010).
13. D. Sirbu, "Occulter-Based High-Contrast Exoplanet Imaging: Design, Scaling, and Performance Verifications", PhD Thesis, Princeton University (2014).
14. W. Cash, "Analytic modeling of starshades", ' Astrophys. J. **738**, (2011).
15. R. Soummer, A. Sivaramakrishnan, and R. J. Vanderbei, "Fast computation of Lyot-style coronagraph propagation", Opt. Express, 15(24), 159345-15951 (2007)
16. T. Glassman, A. Lo, J. Aerenberg, W. Cash, and C. Noecker, "Starshade scaling relations", Proc. SPIE **7440**, 744013 (2009).
17. E. Cady, "Boundary diffraction wave integrals for diffraction modeling of external occulters", Opt. Express **20**(14), 15196-15208 (2012).
18. S. Shaklan, F. Marchen, D. Lisman, E. Cady, S. Martin, N.J. Kasdin, and P. Dumont, "A starshade petal error budget for exo-earth detection and characterization," Proc. SPIE **8151**, 815113 (2011).
19. P. Dumont, S. Shaklan, E. Cady, N.J. Kasdin, and R. Vanderbei, "Analysis of external occulters in presence of defects", Proc. SPIE **7440**, 744008 (2009).
20. D. Sirbu, N. J. Kasdin, and R. Vanderbei, "Monochromatic verification of high-contrast imaging with an occulter", Opt. Express **21**(26), 32234-32253 (2013).
21. K. Balasubramanian, D. Wilson, V. White, R. Muller, M. Dickie, K. Yee, R. Ruiz, S. Shaklan, E. Cady, B. Kern, R. Belikov, O. Guyon, and N. J. Kasdin, "High contrast internal and external coronagraph masks produced by various techniques," Proc. SPIE **8864**, 88641R (2013).
22. J. Goodman, *Introduction to Fourier Optics*, (Roberts & Co., 2005)
23. E. Cady, "Design, Tolerancing, and Experimental Verification of Occulters for Finding Extrasolar Planets", PhD Thesis, Princeton University (2010).
24. D. Sirbu, N. J. Kasdin, and R. Vanderbei, "Diffractive analysis of limits of an occulter experiment," Proc. SPIE **9143**, 91432P (2014).
25. N. J. Kasdin, "Discrete simulation of colored noise and stochastic processes and power law noise generation", Proc. IEEE **83** (1995).
26. M. Born and E. Wolf, *Principles of Optics*, (Cambridge University Press, 1999).
27. M. Rosenblatt, "Remarks on some nonparametric estimates of a density function", Ann. Math. Stat. **27** (1956).
28. E. Parzen, "On estimation of a probability density function and mode", Ann. Math. Stat. **33** (1962).
29. K. Balasubramanian, V. White, K. Yee, P. Echternach, R. Muller, M. Dickie, E. Cady, C. Prada, D. Ryan, I. Poberezhskiy, H. Zhou, B. Kern, A.J. Riggs N. Zimmerman, D. Sirbu, S. Shaklan, and N. J. Kasdin, "Exoplanet coronagraph shaped pupil masks and laboratory scale star shade masks: design, fabrication and characterization," Proc. SPIE **9605**, 96050L (2015).
30. D. Sirbu, S. Shaklan, N. J. Kasdin, and R. Vanderbei, "Scaling relation for occulter manfuacturing errors," Proc. SPIE **9605**, 96052E (2015).
31. Y. Kim, M. Galvin, N. J. Kasdin, R. Vanderbei, D. Ryu, K. Kim, S. Kim, and D. Sirbu, "Design of a laboratory testbed for external occulters at flight Fresnel numbers," Proc. SPIE **9605**, 96052E (2015).